Orbital Edge States in a Photonic Honeycomb Lattice

M. Milićević,[1] T. Ozawa,[2] G. Montambaux,[3] I. Carusotto,[2] E. Galopin,[1] A. Lemaître,[1]
L. Le Gratiet,[1] I. Sagnes,[1] J. Bloch,[1] and A. Amo[1]
[1]*Centre de Nanosciences et de Nanotechnologies, CNRS, Univ. Paris-Sud, Université Paris-Saclay, C2N-Marcoussis, 91460 Marcoussis, France*
[2]*INO-CNR BEC Center and Dipartimento di Fisica, Università di Trento, I-38123 Povo, Italy*
[3]*Laboratoire de Physique des Solides, CNRS, Univ. Paris-Sud, Université Paris-Saclay, 91405 Orsay Cedex, France*

(Received 21 September 2016; published 8 March 2017)

We experimentally reveal the emergence of edge states in a photonic lattice with orbital bands. We use a two-dimensional honeycomb lattice of coupled micropillars whose bulk spectrum shows four gapless bands arising from the coupling of p-like photonic orbitals. We observe zero-energy edge states whose topological origin is similar to that of conventional edge states in graphene. Additionally, we report novel dispersive edge states in zigzag and armchair edges. The observations are reproduced by tight-binding and analytical calculations, which we extend to bearded edges. Our work shows the potentiality of coupled micropillars in elucidating some of the electronic properties of emergent two-dimensional materials with orbital bands.

DOI: 10.1103/PhysRevLett.118.107403

Boundary modes are a fundamental property of finite-size crystals. They play an important role in the electronic transport and in the magnetic properties of low-dimensional materials [1–4]. Their existence has long been related to the microscopic details of the edge of the crystal [5–7]. Recent advances in the study of topological physics have revealed that, for topologically nontrivial materials, the existence of surface states is directly related to the properties of the bulk [8–10]. This is the case of conduction electrons in graphene [11–13], in which the nearest neighbor coupling of the cylindrically symmetric p_z orbitals of the carbon atoms gives rise to two bands (here labeled s bands) crossing in an ungapped spectrum (Dirac cones). The localized edge modes in this system exist for any type of termination except for armchair [14,15]. They are topologically protected by the chiral symmetry of the honeycomb lattice, and their existence can be predicted by calculating the winding number of the bulk wave functions [11–13].

In 2007, Wu and coworkers proposed an orbital version of graphene by considering a honeycomb lattice with $p_{x,y}$ orbitals in each lattice site [16,17]. The strong spatial anisotropy of the orbitals results in four ungapped bands with distinct features: two bands showing Dirac crossings and two flat bands, which were first reported experimentally in a polariton-based photonic simulator [18]. The interest in this kind of orbital Hamiltonian has taken a new thrust due to the rapid emergence of two-dimensional materials [19], such as black phosphorus [20–22] and two-dimensional transition metal dichalcogenides [23], whose bands originate from spatially anisotropic atomic orbitals. Edge states in MoS_2 flakes have been observed [24], and recent works aim at quantifying their impact in the transport properties [25]. Edge states in orbital modes have also been studied theoretically in connection to d-wave superconductivity [11,26] and spin-orbit coupling in superlattices of nanocrystals [27], systems very hard to realize experimentally with tuneable parameters. A photonic simulator of orbital bands would open the door to the study of the microscopic properties of orbital edge states [28] and the connection to the topological properties of orbital bulk bands. In a more general framework, it would provide a platform to simulate some aspects of orbital bands which are essential in various topological insulators with band inversion [29].

In this Letter we report the experimental observation of edge states in the $p_{x,y}$ orbital bands of a honeycomb lattice made out of coupled micropillars etched in a planar microcavity. The advantage of this system over other photonic simulators, such as coupled waveguides [30,31] or microwave resonators [32], is that the radiative emission of light from the micropillars provides direct optical access to both the spatial distribution of the wave functions and to the energy-momentum dispersions [33]. We find two kinds of edge states: (i) zero-energy states in the zigzag and bearded edges, with a topological origin similar to that of edge states in conventional graphene; and (ii) a novel kind of dispersive edge state that emerges not only in zigzag and bearded terminations, but also in armchair edges. We support experimental data with numerical tight-binding calculations and provide analytical expressions for the energy of the dispersive edge states.

To experimentally study orbital edge states in $p_{x,y}$ bands we employ the polaritonic honeycomb lattice reported in [18,34] and shown in Fig. 1(c). The sample is a two-dimensional heterostructure made out of a $Ga_{0.05}Al_{0.95}As$ $\lambda/2$ cavity embedded in two $Ga_{0.05}Al_{0.95}As/Ga_{0.8}Al_{0.2}As$ Bragg mirrors with 28 (40) top (bottom) pairs with twelve GaAs quantum wells grown at the three central maxima of the electromagnetic field

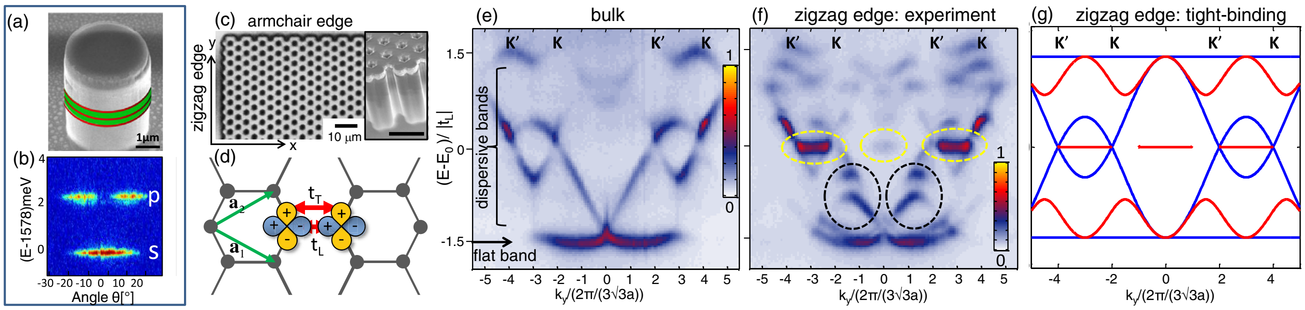

FIG. 1. (a) Scanning electron microscope image of a single micropillar. The red lines sketch the position of the quantum wells embedded in the cavity (depicted in green). (b) Corresponding momentum space spectra showing confined s and p-modes. (c) Optical microscope photograph of the honeycomb lattice under study showing two types of edges. The inset shows a scanning electron microscope image. (d) Sketch of the $p_{x,y}$ orbital (blue and yellow, respectively) and their couplings along the link (t_L) and perpendicular to it (t_T). [(e) and (f)] Momentum space luminescence from the bulk (e) and the zigzag edge (f) for $k_x = 4\pi/(3a)$. K and K' mark the positions of the Dirac cones. Yellow and black dashed lines surround photoluminescence from edge states. $E_0 = 1573$ meV and $t_L = -1.2$ meV. (g) Tight-binding calculation of the band structure. Blue lines, bulk energy bands at $k_x = 4\pi/(3a)$; red lines, edge states obtained for a nanoribbon with zigzag edges. All calculations are for $t_T = 0$.

confined in the heterostructure. The exciton resonance is 17 meV above the cavity mode at $k = 0$, and the exciton photon coupling results in a 15 meV Rabi splitting. After the molecular beam epitaxy growth, the cavity is processed by electron beam lithography and dry etching into a honeycomb lattice of overlapping micropillars (diameter 3 μm, center-to-center distance $a = 2.4$ μm). As shown in Fig. 1(c), both zigzag and armchair terminations were fabricated. The lowest energy level of each micropillar [Figs. 1(a) and 1(b)] is cylindrically symmetric, similarly to the p_z orbitals in graphene. The hopping of photons in these modes [35] gives rise to the π and π^* bands of graphene, whose edge states have been experimentally reported in the same structure [34]. The first excited state is made of two antisymmetric modes, $p_{x,y}$, oriented in orthogonal directions in the horizontal plane, as sketched in Fig. 1(d).

The characterization of the bulk band structure is performed at 10 K in the linear regime by exciting the center of the lattice with a low power (5 mW) nonresonant laser (740 nm), focused on a 4 μm diameter excitation spot. This provides incoherent excitation of all modes with a nonvanishing spatial overlap with the pump. The same microscope objective is used both to excite and to collect the emission [36]. Figure 1(e) displays the photoluminescence spectrum as a function of momentum parallel to the vertical edge, k_y, for $k_x = 4\pi/(3a)$; we select the emission linearly polarized along the same direction. The dispersion shows four bulk bands corresponding to the coupling of the $p_{x,y}$ orbitals (the s bands, lying at lower energy, are not shown) [18]. The lowest band is almost flat, while the two middle ones are strongly dispersive with two band crossings similar to those at the K and K' Dirac points in graphene s bands. The highest energy band corresponds to a deformed flat band [18]. The inhomogeneity in the emitted intensity is the consequence of (i) the energy relaxation efficiency and lifetime of photons in different modes, and (ii) destructive interference in the far-field emission along certain high-symmetry directions [18,38,39]. Such a destructive interference effect is the reason why we select the value of $k_x = 4\pi/(3a)$ instead of the equivalent $k_x = 0$, where the emission intensity is strongly reduced. Tight-binding simulations, including coupling of the photons out of the cavity, nicely reproduce the observed emission pattern [36].

To access the edge states we place the spot on the outermost pillar of the zigzag edge. The measured dispersion is shown in Fig. 1(f). In addition to the bulk modes, new bands are evidenced, marked with yellow and black dashed lines in the figure. Those marked in yellow are flat and show up at the center of both the first and adjacent Brillouin zones, at the energy of the Dirac crossings. Those in black dashed lines lie between the bulk dispersive and flat bands and have a marked dispersive character. These states are delocalized in momentum space in the direction perpendicular to the edge, appearing at the very same energy for any value of k_x (not shown here) and, as we see below, they are localized in real space at the edges. This is different from the bulk bands in Fig. 1(e), which change energy when probing different values of k_x and are delocalized in real space. Note that the polarization dependent confinement of the outermost micropillars [34] and the transverse electric-transverse magnetic (TE-TM) splitting characteristic of semiconductor microcavities [40] may account for the observed splitting in the lowest flat band and in the edge states at around $k_y = \pm 1.5[2\pi/(3\sqrt{3}a)]$, black dashed lines in Fig. 1(f).

The $p_{x,y}$ orbital bands can be described by a tight-binding Hamiltonian [17,18]. If we assume that only the hopping via orbitals projected along the links connecting the micropillars is significant $|t_L| \gg |t_T|$, see Fig. 1(d), the Hamiltonian in the a_x, a_y, b_x, b_y basis, corresponding to the $p_{x,y}$ orbitals of the A and B sublattices, can be written in momentum space in the following 4×4 form:

$$\hat{\mathcal{H}}_p = -t_L \begin{pmatrix} 0_{2\times2} & Q^\dagger \\ Q & 0_{2\times2} \end{pmatrix}, \quad \text{with}$$

$$Q = \begin{pmatrix} f_1 & g \\ g & f_2 \end{pmatrix}, \tag{1}$$

where $f_1 = \frac{3}{4}(e^{i\mathbf{k}\cdot\mathbf{u}_1} + e^{i\mathbf{k}\cdot\mathbf{u}_2})$, $f_2 = 1 + \frac{1}{4}(e^{i\mathbf{k}\cdot\mathbf{u}_1} + e^{i\mathbf{k}\cdot\mathbf{u}_2})$, and $g = (\sqrt{3}/4)(e^{i\mathbf{k}\cdot\mathbf{u}_1} - e^{i\mathbf{k}\cdot\mathbf{u}_2})$; $\mathbf{u}_{1,2}$ are primitive vectors and $t_L < 0$, to account for the antisymmetric phase distribution of the p orbitals. To later describe finite-size samples, we make a choice of unit cell dimer and primitive vectors such that it allows the full reconstruction of the lattice including its specific edges. We take the primitive vectors as follows: $\mathbf{u}_1 = \mathbf{a}_1$, $\mathbf{u}_2 = \mathbf{a}_1 - \mathbf{a}_2$ for zigzag edges, and $\mathbf{u}_1 = \mathbf{a}_1$, $\mathbf{u}_2 = \mathbf{a}_2$ for bearded and armchair, given in terms of the reference vectors $\mathbf{a}_{1,2}$ defined in Fig. 1(d); the corresponding unit cell dimers are detailed in Ref. [36].

The diagonalization of Hamiltonian (1) gives rise to two flat bands with energies $\pm\frac{3}{2}t_L$, and two dispersive bands with energies $\pm\frac{2}{3}t_L|\det Q|$, that is [16]

$$\pm\frac{t_L}{2}\sqrt{3 + 2\cos(\sqrt{3}k_y a) + 4\cos(3k_x a/2)\cos(\sqrt{3}k_y a/2)}. \tag{2}$$

Figures 1(e) and 1(f) are well described by a value of $t_L = -1.2$ meV, significantly larger than the measured linewidth ($\approx$150 μeV) and on-site energy disorder ($\approx$30 μeV, as measured in a similar one-dimensional structure [41]). To account for the edge bands experimentally reported in Fig. 1(f) we compute the eigenmodes of Hamiltonian (1) in a finite-size sample. We consider a nanoribbon with zigzag terminations on both edges and periodic boundary conditions along the direction parallel to the edge. The bulk modes, blue lines in Fig. 1(g), are the analytic result [Eq. (2)] and are delocalized all over the ribbon, while the red lines in Fig. 1(g) are edge states, calculated on a finite-size system, whose wave function exponentially decays. The spread in momentum and the position in energy match quantitatively the experimental observations, particularly for the modes at and below the Dirac cones. In the experiment, the high energy part of the spectrum is deformed due to the coupling to higher modes, and to the nonzero value of t_T, whose strength increases with energy [18].

Tight-binding calculations for nanoribbons with zigzag, bearded, and armchair edges are shown in Fig. 2. Two kinds of edge modes are visible: (i) bands of zero-energy modes in the central gap, present in zigzag and bearded edges, and (ii) dispersive modes in the upper and lower gaps in all three types of edges, and in the middle gap of the armchair termination.

We first analyze the zero-energy edge modes. They recall strongly the edge modes in the π and π^* bands of regular graphene, whose existence can be related to the winding number of the wave functions in momentum space [11–13]. The Hamiltonian describing graphene (s bands) is a chiral 2×2 Hamiltonian,

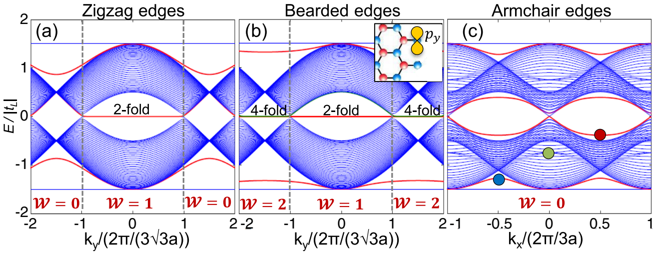

FIG. 2. Calculated eigenmodes in the first Brillouin zone for a nanoribbon as a function of the wave vector $k_\parallel$ parallel to the edges, with (a) zigzag ($k_\parallel = k_y$), (b) bearded ($k_\parallel = k_y$), and (c) armchair ($k_\parallel = k_x$) terminations. Blue curves: bulk spectra for different values of the transverse momentum $k_\perp$. Red and green curves: edge states. For bearded edges, the inset shows the uncoupled p_y orbitals that give rise to a pair of edge states spreading over all $k_\parallel$.

$$\hat{\mathcal{H}}_s = -t_s \begin{pmatrix} 0 & f_s^* \\ f_s & 0 \end{pmatrix}, \tag{3}$$

with $t_s > 0$ being the hopping amplitude for the s orbitals and the factor $f_s = 1 + e^{i\mathbf{k}\cdot\mathbf{u}_1} + e^{i\mathbf{k}\cdot\mathbf{u}_2}$. The unit cell vectors $\mathbf{u}_{1,2}$ contain the information about the considered edge, as discussed above. The number of zero-energy edge states is determined by the winding of the phase of the off-diagonal component [$f_s = |f_s|e^{i\phi(\mathbf{k})}$] [11–13],

$$\mathcal{W}(k_\parallel) = \frac{1}{2\pi}\int_{BZ}\frac{\partial\phi(\mathbf{k})}{\partial k_\perp}dk_\perp, \tag{4}$$

where the one-dimensional integration over $k_\perp$ is performed along a loop around the Brillouin zone in a direction perpendicular to the considered edge.

This analysis can be extended to more general situations: the existence of zero-energy modes can be related to the winding properties of the Hamiltonian in the following way. By fixing a value of $k_\parallel$, the dependence of Hamiltonian (1) on $k_\perp$ can be regarded as a one-dimensional model in the BDI (chiral orthogonal) class of the classification of topological insulators introduced by Schnyder *et al.* [10]. For this class, the number of pairs of zero-energy edge modes is given by the winding of the phase ϕ obtained from $f_p \equiv \det Q = |\det Q|e^{i\phi(\mathbf{k})}$ [42]. Figure 2 shows the value of $\mathcal{W}(k_\parallel)$ for the p bands as a function of momenta parallel to the edge $k_\parallel$ for the three types of edge considered here [36]. The winding number $\mathcal{W}(k_\parallel)$ matches with the number of the zero-energy modes calculated by diagonalization of the Hamiltonian.

An interesting feature of Fig. 2 is that the regions in momentum space where the zero-energy modes are present in the zigzag edge ($k_\parallel \in [-2\pi/(3\sqrt{3}a), 2\pi/(3\sqrt{3}a)]$) are complementary to the regions in which they are present in s-band graphene for the same kind of edge ($k_\parallel \notin [-2\pi/(3\sqrt{3}a), 2\pi/(3\sqrt{3}a)]$). A similar situation takes place for the bearded edges: in the p bands, pairs of edge modes appear in the region in k space complementary to the regions where they appear in the s bands. Additionally, for bearded terminations, the p bands show an extra pair of zero-energy edge modes spread all over $k_\parallel$. It arises from dangling p_y orbitals fully localized in the outermost pillars, uncoupled to the bulk, as sketched in the inset of Fig. 2(b), and adds to the pair of edge states discussed above. The armchair edge does not have any zero-energy edge mode.

The complementarity in the position in momentum space of zero-energy edge modes between s and p bands can be understood by analyzing the symmetry of Hamiltonians (1) and (3), for the p and the s bands, respectively. The expressions f_p and f_s, whose winding determines the existence of zero-energy edge modes, can be related analytically,

$$f_p(\text{zigzag}) = \frac{3}{4} e^{i\mathbf{k}\cdot(\mathbf{a}_1-\mathbf{a}_2)} f_s(\text{bearded}) \tag{5}$$

$$f_p(\text{bearded}) = \frac{3}{4} e^{i\mathbf{k}\cdot\mathbf{a}_2} f_s(\text{zigzag}), \tag{6}$$

where $f_s(\text{zigzag})[f_p(\text{bearded})]$ is written using the choice of unit cell that corresponds to the zigzag (bearded) edge [13]. A consequence of Eq. (5) is that the winding of the phase of $f_p(\text{zigzag})$ is the same as of $f_s(\text{bearded})$ [the vector $\mathbf{a}_1 - \mathbf{a}_2$ is parallel to the edge, so the prefactor of the right-hand part of Eq. (5) gives no winding in the orthogonal direction]. A similar situation takes place for Eq. (6): in addition to the exchange of the position between zigzag and bearded edge states, of respectively, s and p bands, the phase factor $e^{i\mathbf{k}\mathbf{a}_2}$ provides an extra winding over the whole Brillouin zone, and gives rise to an extra pair of edge state for all values of k_x, in the bearded edges of the p bands.

One of the most distinctive features of Figs. 1 and 2 is the observation of additional dispersive edge modes between the dispersive and the flat bands of the bulk. These modes are present for all values of $k_\parallel$ and for all the investigated types of edges. We can obtain analytical expression of the dispersive edge modes by searching for solutions of the Hamiltonian with an exponential decay into the bulk [$\psi(x) \sim e^{-x/\xi}$, ξ being the penetration length], using the treatment described in Refs. [2,32]. Applying this method to zigzag and bearded edges, we find the following eigenenergies for the edge modes [36]:

$$E^{\text{zigzag}}_{\text{disp edge}}(k_\parallel) = \pm t_L \frac{\sqrt{3}}{2} \sqrt{2 + \cos(\sqrt{3}k_\parallel a)} \tag{7}$$

$$E^{\text{bearded}}_{\text{disp edge}}(k_\parallel) = \pm t_L \frac{\sqrt{3}}{2} \frac{\sqrt{5 - 2\cos(\sqrt{3}k_\parallel a)}}{\sqrt{2 - \cos(\sqrt{3}k_\parallel a)}}. \tag{8}$$

As evidenced in Fig. 2(c), dispersive edge states exist also for armchair terminations, which do not contain any edge modes in the case of regular electronic graphene. The analytic calculation for the armchair edges is more elaborate [43]: the decay of the wave function is not a simple exponential but it involves two different penetration lengths.

We take advantage of our photonic simulator to explore the spatial distribution of these novel edge modes. Figure 3 shows the real space emission from the photonic simulator excited close to the armchair edge for three emission energies, corresponding to three different dispersive edge states indicated in Fig. 2(c) (see Ref. [36] for the experimental dispersion of the armchair edge modes). We employ a pump spot of 20 μm in diameter, allowing the measurement of the wave functions of the edge modes, which penetrate several microns into the bulk.

For the lowest-energy dispersive edge state [Fig. 3(a)], the emission is localized in the second to the last row of micropillars, with a gradual decrease towards the bulk. These features along with the lobe structure are well reproduced by the plot of the tight-binding solution for the edge state at the corresponding energy [$k_x = \pi/(3a)$; Fig. 3(d)]. Figure 3(b) shows the emission pattern for the lowest-energy edge mode in the central gap. In this case, the outermost pillars show the highest intensity, in a pattern significantly different from the modes shown in Figs. 3(a) and 3(d). It is worth noting that in the experiment, the energy of the emission is filtered with the use of a spectrometer, but no particular in-plane momentum is selected. Therefore, bulk modes contribute to the emission at the energies studied in Figs. 3(a)–3(c), explaining the

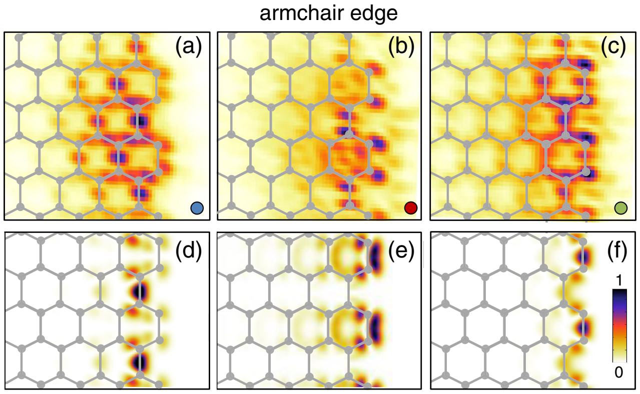

FIG. 3. Real space emission from dispersive edge states in an armchair termination. [(a)–(c)] Measured photoluminescence when selecting the energies indicated with circles in Fig. 2(c). [(d)–(f)] Corresponding tight-binding eigenfunctions. A hexagonal lattice is sketched on top of the data to mark the position of the center of the micropillars.

differences with the calculated individual eigenfunctions depicted in Figs. 3(d)–3(f).

Interestingly, the tight-binding calculations in Fig. 2(c) reveal an additional edge mode within the bulk energy band (green dot). Despite being immersed in the bulk band, when selecting the emission at the highest energy of this mode, the experiment and tight-binding calculations shown in Figs. 3(c) and 3(f) attest to the significant localization of these modes in the edge region.

In summary, our results provide a detailed characterization of the zero-energy and dispersive orbital edge states in excited bands of a photonic honeycomb lattice. The zero-energy modes are well described using topological arguments based on the symmetries of the bulk Hamiltonian. Whether any topological argument can be applied to the dispersive edge modes is an intriguing question. Our experiments and theoretical analysis provide insights into multimode lattice systems such as transition metal dichalcogenides [23] or mechanical lattices of springs and masses, which have been predicted to show similar dispersive edge modes [42,44]. Taking advantage of the intrinsic nonlinearities of polaritons, honeycomb lattices of coupled micropillars appear as excellent candidates to explore nonlinear bulk and edge states with orbital structure [45].

This work was supported by the French National Research Agency (ANR) program Labex NanoSaclay via the projects Qeage (Grant No. ANR-11-IDEX-0003-02) and ICQOQS (Grant No. ANR-10-LABX-0035), the French RENATECH network, the ERC grants Honeypol and QGBE, the EU-FET Proactiv grant AQUS (Project No. 640800), and by the Provincia Autonoma di Trento, partially through the project “On silicon chip quantum optics for quantum computing and secure communications—SiQuro”.

[1] K. Nakada, M. Fujita, G. Dresselhaus, and M. S. Dresselhaus, Phys. Rev. B **54**, 17954 (1996).
[2] M. Kohmoto and Y. Hasegawa, Phys. Rev. B **76**, 205402 (2007).
[3] Y. Li, Z. Zhou, S. Zhang, and Z. Chen, J. Am. Chem. Soc. **130**, 16739 (2008).
[4] Y. Li, W. Zhang, M. Morgenstern, and R. Mazzarello, Phys. Rev. Lett. **110**, 216804 (2013).
[5] W. Shockley, Phys. Rev. **56**, 317 (1939).
[6] I. Tamm, Zeitschrift für Physik **76**, 849 (1932).
[7] J. Zak, Phys. Rev. B **32**, 2218 (1985).
[8] M. Z. Hasan and C. L. Kane, Rev. Mod. Phys. **82**, 3045 (2010).
[9] X.-L. Qi and S.-C. Zhang, Rev. Mod. Phys. **83**, 1057 (2011).
[10] A. P. Schnyder, S. Ryu, A. Furusaki, and A. W. W. Ludwig, Phys. Rev. B **78**, 195125 (2008).
[11] S. Ryu and Y. Hatsugai, Phys. Rev. Lett. **89**, 077002 (2002).
[12] R. S. K. Mong and V. Shivamoggi, Phys. Rev. B **83**, 125109 (2011).
[13] P. Delplace, D. Ullmo, and G. Montambaux, Phys. Rev. B **84**, 195452 (2011).
[14] Y. Kobayashi, K.-i. Fukui, T. Enoki, K. Kusakabe, and Y. Kaburagi, Phys. Rev. B **71**, 193406 (2005).
[15] J. Lado, N. García-Martínez, and J. Fernández-Rossier, Synth. Met. **210**, 56 (2015).
[16] C. Wu, D. Bergman, L. Balents, and S. Das Sarma, Phys. Rev. Lett. **99**, 070401 (2007).
[17] C. Wu and S. Das Sarma, Phys. Rev. B **77**, 235107 (2008).
[18] T. Jacqmin, I. Carusotto, I. Sagnes, M. Abbarchi, D. D. Solnyshkov, G. Malpuech, E. Galopin, A. Lemaître, J. Bloch, and A. Amo, Phys. Rev. Lett. **112**, 116402 (2014).
[19] S. Z. Butler, S. M. Hollen, L. Cao, Y. Cui, J. A. Gupta, H. R. Gutiérrez, T. F. Heinz, S. S. Hong, J. Huang, A. F. Ismach, E. Johnston-Halperin, M. Kuno, V. V. Plashnitsa, R. D. Robinson, R. S. Ruoff, S. Salahuddin, J. Shan, L. Shi, M. G. Spencer, M. Terrones, W. Windl, and J. E. Goldberger, ACS Nano **7**, 2898 (2013).
[20] J.-H. P. Churchill and O. H. Hugh, Nat. Nanotechnol. **9**, 330 (2014).
[21] L. Li, Y. Yu, G. J. Ye, Q. Ge, X. Ou, H. Wu, D. Feng, X. H. Chen, and Y. Zhang, Nat. Nanotechnol. **9**, 372 (2014).
[22] X. Ling, H. Wang, S. Huang, F. Xia, and M. S. Dresselhaus, Proc. Natl. Acad. Sci. U.S.A. **112**, 4523 (2015).
[23] K. S. Novoselov, A. Mishchenko, A. Carvalho, and A. H. Castro Neto, Science **353** (2016).
[24] M. V. Bollinger, J. V. Lauritsen, K. W. Jacobsen, J. K. Nørskov, S. Helveg, and F. Besenbacher, Phys. Rev. Lett. **87**, 196803 (2001).
[25] M. Trushin, E. J. R. Kelleher, and T. Hasan, Phys. Rev. B **94**, 155301 (2016).
[26] S. Ryu and Y. Hatsugai, Physica (Amsterdam) **388C**, 90 (2003).
[27] E. Kalesaki, C. Delerue, C. Morais Smith, W. Beugeling, G. Allan, and D. Vanmaekelbergh, Phys. Rev. X **4**, 011010 (2014).
[28] C. Segarra, J. Planelles, and S. E. Ulloa, Phys. Rev. B **93**, 085312 (2016).
[29] B. A. Bernevig, T. L. Hughes, and S.-C. Zhang, Science **314**, 1757 (2006).
[30] Y. Plotnik, M. C. Rechtsman, D. Song, M. Heinrich, J. M. Zeuner, S. Nolte, Y. Lumer, N. Malkova, J. Xu, A. Szameit, Z. Chen, and M. Segev, Nat. Mater. **13**, 57 (2014).
[31] M. Hafezi, S. Mittal, J. Fan, A. Migdall, and J. M. Taylor, Nat. Photonics **7**, 1001 (2013).
[32] M. Bellec, U. Kuhl, G. Montambaux, and F. Mortessagne, New J. Phys. **16**, 113023 (2014).
[33] I. Carusotto and C. Ciuti, Rev. Mod. Phys. **85**, 299 (2013).
[34] M. Milićević, T. Ozawa, P. Andreakou, I. Carusotto, T. Jacqmin, E. Galopin, A. Lemaître, L. Le Gratiet, I. Sagnes, J. Bloch, and A. Amo, 2D Mater. **2**, 034012 (2015).
[35] M. Galbiati, L. Ferrier, D. D. Solnyshkov, D. Tanese, E. Wertz, A. Amo, M. Abbarchi, P. Senellart, I. Sagnes, A. Lemaitre, E. Galopin, G. Malpuech, and J. Bloch, Phys. Rev. Lett. **108**, 126403 (2012).
[36] See Supplemental Material at http://link.aps.org/supplemental/10.1103/PhysRevLett.118.107403, which includes Ref. [37], for a description of the experimental setup, measured dispersions for the armchair edge, driven-dissipative simulations, and analytical results on the dispersion of zigzag and bearded edge states.

[37] T. Ozawa and I. Carusotto, Phys. Rev. Lett. **112**, 133902 (2014).

[38] E. L. Shirley, L. J. Terminello, A. Santoni, and F. J. Himpsel, Phys. Rev. B **51**, 13614 (1995).

[39] A. Bostwick, T. Ohta, T. Seyller, K. Horn, and E. Rotenberg, Nat. Phys. **3**, 36 (2007).

[40] G. Panzarini, L. C. Andreani, A. Armitage, D. Baxter, M. S. Skolnick, V. N. Astratov, J. S. Roberts, A. V. Kavokin, M. R. Vladimirova, and M. A. Kaliteevski, Phys. Rev. B **59**, 5082 (1999).

[41] F. Baboux, L. Ge, T. Jacqmin, M. Biondi, E. Galopin, A. Lemaître, L. Le Gratiet, I. Sagnes, S. Schmidt, H. E. Türeci, A. Amo, and J. Bloch, Phys. Rev. Lett. **116**, 066402 (2016).

[42] C. L. Kane and T. C. Lubensky, Nat. Phys. **10**, 39 (2013).

[43] T. Ozawa *et al.* (to be published).

[44] Y.-T. Wang, P.-G. Luan, and S. Zhang, New J. Phys. **17**, 073031 (2015).

[45] M. Di Liberto, A. Hemmerich, and C. Morais Smith, Phys. Rev. Lett. **117**, 163001 (2016).